

Article

# Effect of Hot Band on Texture Evolution and Plastic Anisotropy in Aluminium Alloys

Jurij J. Sidor 

Savaria Institute of Technology, Faculty of Informatics, Eötvös Loránd University (ELTE), Károlyi Gáspár tér 4, 9700 Szombathely, Hungary; js@inf.elte.hu

**Abstract:** This contribution presents the evolution of crystallographic texture during thermomechanical processing of Al alloys. It is shown that the nature of crystallographic changes involved in deformation and recrystallization is strongly affected by the variety of initial (pre-rolling) state of a given metallic system. Four hot rolled Al strips of identical chemical composition and different textures were subjected to further thermomechanical processing with equal technological characteristics. Although the pre-rolling textures were first destroyed by the deformation, while annealing accounted for further qualitative and quantitative crystallographic changes in the investigated polycrystalline systems, it seems that there is still a great influence of the hot band texture on the texture dependent properties. Various qualitative and quantitative texture characteristics of annealed sheets ensured diverse Lanford value curves, which is a direct consequence of the crystallographic features developed in the hot bands. The Cube-dominated hot band ensured a strong V-shaped profile after cold rolling and subsequent recrystallization, whereas it was shown that a weak pre-rolling texture is more advantageous in terms of both normal and planar anisotropy.

**Keywords:** texture; hot band; Al alloys; anisotropy; processing; Lankford value



**Citation:** Sidor, J.J. Effect of Hot Band on Texture Evolution and Plastic Anisotropy in Aluminium Alloys. *Metals* **2021**, *11*, 1310. <https://doi.org/10.3390/met11081310>

Academic Editor: Beatriz López Soria

Received: 18 July 2021

Accepted: 3 August 2021

Published: 19 August 2021

**Publisher's Note:** MDPI stays neutral with regard to jurisdictional claims in published maps and institutional affiliations.



**Copyright:** © 2021 by the author. Licensee MDPI, Basel, Switzerland. This article is an open access article distributed under the terms and conditions of the Creative Commons Attribution (CC BY) license (<https://creativecommons.org/licenses/by/4.0/>).

## 1. Introduction

Polycrystalline metal sheets are generally produced by casting, rolling, annealing and these thermomechanical processes (TMP) ensure continuous structural rearrangements on various levels [1,2]. The majority of resulting properties are strongly dependent on the crystal structure of metallic systems, alloying elements, evolved grain size, and homogeneity of microstructure, while others are affected by the crystallographic texture, which tends to evolve during the entire TMP process [1]. In the case of Al alloys, the TMP involves direct chill casting, homogenization, which is followed by the hot and cold rolling (in some instances intermediate annealing is employed between the rolling passes) and finally the deformed material is subjected to annealing, that induces recovery and/or partial/full recrystallization (RX). Each stage of the TMP chain was studied in great detail and can be considered as an independent event. However, the results of numerous investigations clearly show that there is a kind of “hereditary” connection between the individual processing steps [1–6]. The apparent interconnection between the distinct links of the production chain implies that each TMP step affects the consequent process and likewise the final properties of a given material. The metallic polycrystalline systems exposed to a sequence of rolling and heat treatment processes tend to experience morphological changes, which depend on the technological parameters, such as the degree of straining level, deformation rate, annealing history etc. Typically, single-phase microstructures retain a trace of the preceding TMP steps via the grain size and morphology, microstructure heterogeneity, linear and two-dimensional defects evolved within particular grains, as well as the evolution of dominant crystallographic orientations or orientation fibres in the polycrystalline aggregate. The crystallographic aspect of mesoscopic changes is far more complex and less apparent compared to morphologic one, inasmuch as a set of new orientations replaces the preceding texture and the link between the two qualitatively different

counterparts is not straightforward [1,2,5,6]. For instance, in metals with face-centered cubic (FCC) crystal structure, the deformation texture is characterized by the  $\alpha$  and  $\beta$  fibres (see Figure 1), whereas at higher straining levels, the majority of orientations are aligned along the  $\beta$ -fibre [7], which connects the Copper and Brass components via the following set of orientations:  $\{325\}\langle 10\ 15\ 12\rangle$ ,  $\{213\}\langle 9\ 15\ 11\rangle$ ,  $\{314\}\langle 5\ 9\ 6\rangle$  [8]. During discontinuous annealing, the deformation texture components tend to transform to a qualitatively new one [1,2], characterized by the  $\theta$  and  $\eta$ -fibre orientations mixed with the weakly developed  $\alpha$  and  $\gamma$ -fibre orientations.

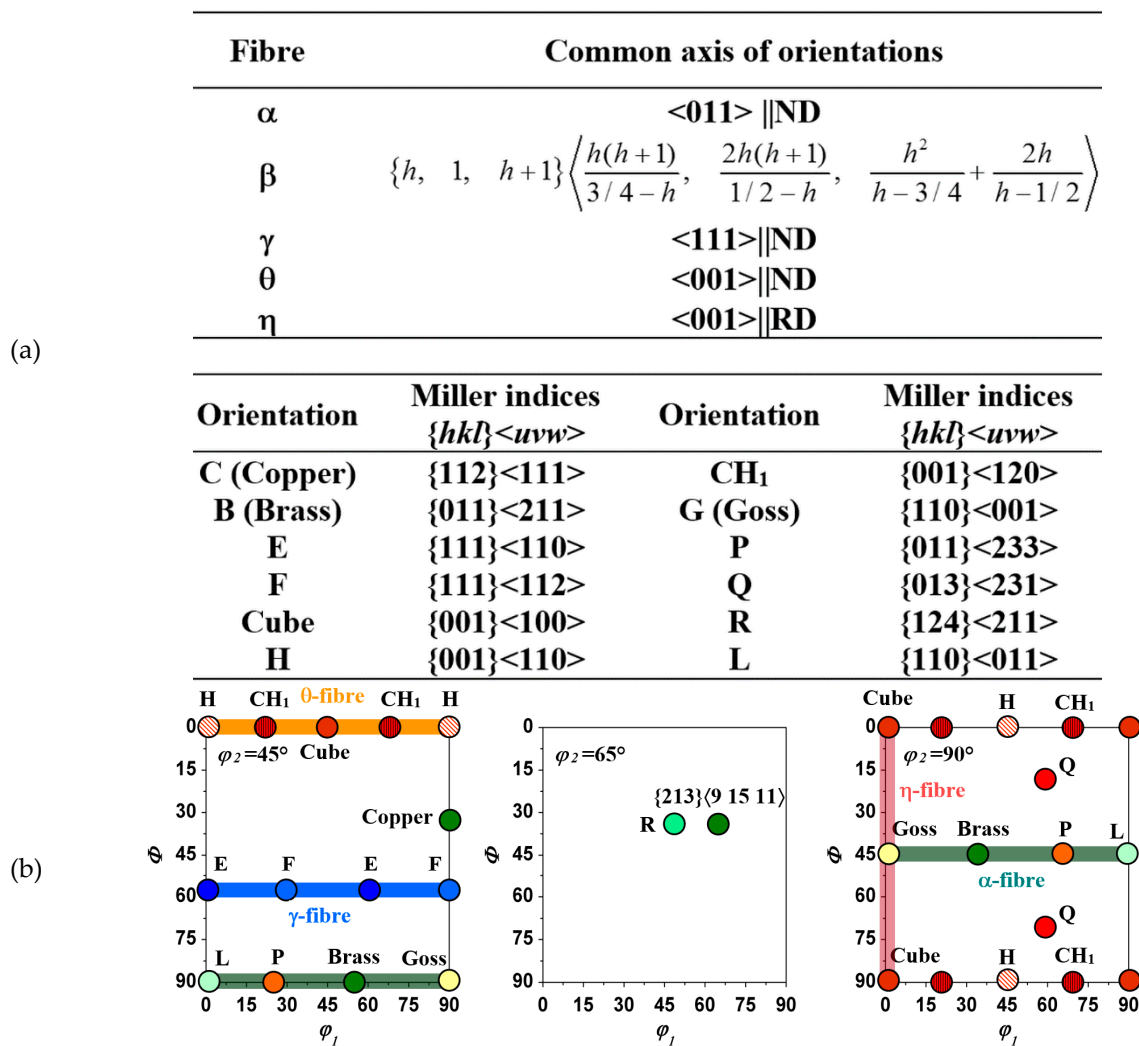


**Figure 1.** Crystallographic orientations and fibres, which tend to appear during thermomechanical processing of Al alloys and other materials with FCC crystal structure (RD, ND and TD stand for rolling, normal and transverse directions, respectively): (a) Miller indices of fibres and orientations; (b)  $\varphi_2 = 45^\circ$ ,  $\varphi_2 = 65^\circ$ , and  $\varphi_2 = 90^\circ$  sections of Euler space.

Briefly summarizing the TMP of Al alloys, it should be mentioned that Al ingots are typically reheated to elevated temperatures (reheating temperature is alloy dependent and generally above 500 °C) and transferred to the breakdown unidirectional or reversible hot rolling mill while this process is followed by a high-speed tandem rolling [1–3]. The severe thickness reductions involved (above 98%), elevated temperatures, and large inter-pass times between two consecutive rolling passes tend to induce static recrystallization in the breakdown rolling and lead to the evolution of Cube orientation [9]. The succeeding high-speed rolling by the tandem mill diminishes the importance of interpass recrystallization, however, the so-called self-annealing can take place during the coiling of the hot rolled strip [9,10]. The wide variety of hot rolling processing parameters results in a vast diversity

of microstructures and textures, which tend to develop in the hot band [2–4,10,11]. As it was claimed in Ref [2], low finishing temperature ( $T < 240\text{ }^{\circ}\text{C}$ ) in the uncoiled strip ensures relatively homogeneous microstructure with highly elongated grains along rolling direction (RD), while the texture is composed of a mixture of  $\beta$ -fibre and very weak Cube and Goss RX texture components. The hot rolled and subsequently coiled strip showed a similar microstructural evolutionary pattern [2], however, the crystallographic texture contained a significantly higher volume fraction of RX components mixed with the characteristic rolling texture fibres. Results of investigations suggest that the evolution of RX texture components at low roll finishing temperatures ( $T \sim 250\text{ }^{\circ}\text{C}$ ) could be attributed to the enhanced interpass time which triggers recrystallization process, while the increase of the roll finishing temperatures ( $T > 300\text{ }^{\circ}\text{C}$ ) may account for complete recrystallization in the coiled strips because of a self-annealing [10]. In summary, one can conclude that three qualitatively different texture types might evolve during hot rolling: (i)  $\beta$ -fibre dominating texture, (ii)  $\beta$ -fibre mixed with RX components, and (iii) purely RX texture components if the HB coil is subjected to annealing at elevated temperature.

Controlling both the microstructure and texture evolution during hot rolling is an important technological challenge, inasmuch as the microstructural features of the hot band significantly contribute to the development of properties in the final state [3,4,9–11]. Since the texture is a major source of anisotropy [12,13], it is of key importance to produce a material with proper crystallographic features to ensure corresponding material's behavior during the post-processing operations such as forming, deep drawing or stamping. Both normal and planar anisotropy (average  $r$  and  $\Delta r$ ), calculated from the Lankford values, measured in tension at different angles with respect to RD, are indicative of forming qualities of flat materials. Ideally, the average Lankford value should be as highest as possible (or above 1) to avoid thinning of a sheet while the measured in-plane diversities should be minimized to the lowest possible level. As has already been proven [1,2,12,14–16], both normal and planar anisotropy values are directly related to the texture evolved during the last step of TMP, and therefore texture control during each TMP step is of particular relevance since the texture development is a continuous evolutionary process throughout the production chain.

The materials research community continues aiming to understand the relationships between the TMP and microstructure evolution in metallic systems [4–7,9,14–17], and in that context, this contribution presents the through process texture evolution in 6xxx Al alloy with diverse hot bands and shade a light on the effect of HB texture on plastic strain ratio.

## 2. Materials and Methods

In order to reveal the effect of hot band texture on plastic anisotropy, four samples of Al-Mg-Si alloy (AA6016 series) with identical chemical composition and diverse prerolling textures were subjected to detailed investigation. The evolution of crystallographic texture was studied in samples A–D. The first sample (A) was subjected to non-conventional asymmetric hot rolling, while the other three counterparts (B–D) were symmetrically hot rolled. Diversity of TMP parameters prior to cold rolling ensured different hot band textures. All hot band strips were cold rolled with 86% thickness reduction and afterward, the deformed sheets were heat-treated at  $550\text{ }^{\circ}\text{C}$  for 30 s with the aim to ensure a fully recrystallized state.

The hot band, cold rolled and annealed samples were exposed to textures measurements across the thickness by electron backscattering diffraction (EBSD) technique, which enables relatively fast data collection rates and accurate pattern indexing. In the case of hot rolled and annealed samples, the EBSD detector (EDAX Inc., Mahwah, NJ, USA) was optimized for high data collection at  $\sim 100$  frames per second while the deformed samples were investigated at a lower acquisition speed  $\sim 10$  frames per second. In each case, the orientation data were gained from the plane perpendicular to the sample transverse direction (TD-plane). The electron backscatter patterns were collected and post-processed

by the commercial OIM-TSL-8<sup>®</sup> software (EDAX Inc., Mahwah, NJ, USA). The orientation imaging microscopy (OIM) data were acquired by the Hikari-type<sup>®</sup> detector (EDAX Inc., Mahwah, NJ, USA), which was attached to the high-resolution scanning electron microscope (FEG-SEM) FEI-TENE0<sup>®</sup> (Thermo Fisher Scientific, Brno, Czech Republic). The EBSD data of both hot rolled and annealed materials were collected at the acceleration voltages of 18–20 kV. In the deformed materials, the acquisition was performed at lower acceleration voltages, to avoid overlapping of acquired patterns with ones originating from the deeper layers. Application of 14–18 kV guaranteed appropriate pattern quality. During OIM measurements, the investigated samples were 70° tilted with respect to the EBSD detector. The EBSD mapping was conducted on hexagonal scan grids. The experimentally measured orientation distribution functions (ODFs) were displayed in the  $\varphi_2 = 45^\circ$ ,  $\varphi_2 = 65^\circ$  and  $\varphi_2 = 90^\circ$  sections respectively, which reveal the majority of texture components and fibres evolving during both deformation and annealing.

The quantitative characteristics of texture evolution are discussed in terms of ODF maximum value ( $ODF_{max}$ , expressed in multiples of random distribution, m.r.d.), texture index (integrated intensity value of all orientation in Euler space,  $TI = \int f(g)dg$ ), and distribution of texture components along the fibres (see Figure 1), which are characteristic for a given process.

Sample preparation for OIM examination was performed according to the standard procedure, which comprises mechanical grinding, polishing as well as electrolytic polishing. The mechanical polishing procedure was finished with two DiaDuo Struers<sup>®</sup>-type (Struers, Denmark) suspensions which contain 3 and 1  $\mu\text{m}$  diamond particles, respectively. After obtaining a mirror-type surface quality, the samples were cleaned with liquid soap and rinsed with warm water. As a final step of sample preparation for EBSD, the clean and dry surfaces of investigated samples A–D were subjected to the electrolytic polishing (with A2 Struers<sup>®</sup> electrolyte (Struers, Denmark)), which was conducted for 45–60 s at voltages ranging from 20 to 30 V. The A2 electrolyte was cooled to temperatures ranging between  $-5$  and  $0^\circ\text{C}$ .

To assess the effect of annealing texture on both normal and planar anisotropy, the Lankford value profiles were simulated for samples A–D by a well-established crystal plasticity model Alamel [18,19]. The calculation of  $r$ -values was performed with the model by taking into account the  $\{111\}\langle 110\rangle$  octahedral slip systems, which typically operate during deformation at room temperatures in materials with FCC crystal structure.

### 3. Results and Discussion

#### 3.1. Hot Band Texture

Prior to cold rolling, the investigated materials A–D were subjected to complex TMP, which involved both conventional and non-conventional processing strategies. The evolution of crystallographic texture during hot rolling is beyond the scope of this contribution, nevertheless, a brief summary of HB textures developed is presented below. As can be seen in Figure 2, two distinct types of textures evolved after hot deformation. The asymmetric hot rolling tended to produce an ODF with broken orthotropic sample symmetry. Given this, the texture of Figure 2a was calculated by employing triclinic symmetry ( $0 \leq \varphi_1 \leq 360^\circ$ ,  $0 \leq \Phi \leq 90^\circ$ ,  $0 \leq \varphi_2 = 90^\circ$ ) to reveal the true nature of texture evolution during the non-conventional processing. In contrast to sample A, the rest of investigated samples (B–D) were subjected to conventional/symmetric hot rolling and therefore the application of orthotropic symmetry ( $0 \leq \varphi_1 \leq 90^\circ$ ,  $0 \leq \Phi \leq 90^\circ$ ,  $0 \leq \varphi_2 = 90^\circ$ ) is justified. The ODFs presented in Figure 2a–d reveal significant qualitative and quantitative diversities. Material A is characterized by the asymmetric texture of moderate intensity (the maximum ODF value  $ODF_{max}$  is 6.47 m.r.d.) and orientations, which were spread around the  $\alpha$  and  $\theta$  fibres mixed with the traces of components scattered around the  $\beta$ -fibre. Compared to conventionally produced materials B–D, the texture components evolved in material A are significantly shifted from the fibres (see Figure 1), which tended to develop during symmetric hot rolling.

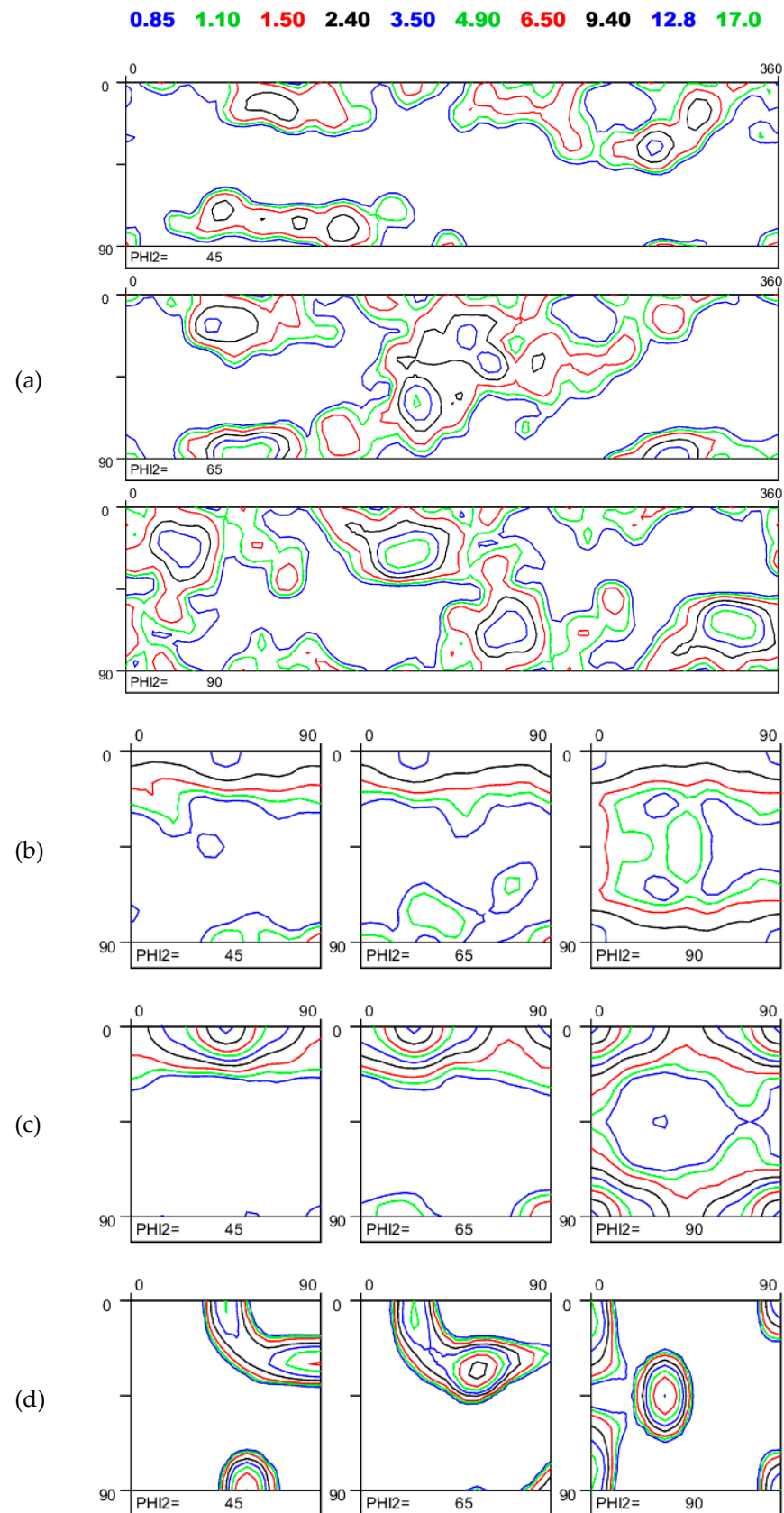


**Figure 2.** Hot band textures observed in the investigated materials: (a) material A,  $ODF_{max} = 6.47$ ,  $TI = 1.98$ ; (b) material B,  $ODF_{max} = 3.92$ ,  $TI = 1.34$ ; (c) material C,  $ODF_{max} = 13.94$ ,  $TI = 2.63$ ; (d) material D,  $ODF_{max} = 11.83$ ,  $TI = 4.24$ .

The ODFs of conventionally hot rolled materials B–D consist of components distributed along the  $\alpha$ ,  $\beta$ ,  $\theta$ ,  $\eta$  fibres. Figure 2a shows the faintly developed texture of material B, which is characterized by quite consistent  $\theta$ -fibre (ND rotated cube orientations) with a maximum intensity of 3.92 m.r.d. at  $\{001\}\langle 100\rangle$  orientation, weak RD rotated cube components and  $\alpha$ -fibre orientations, such as Goss and Brass. Both  $TI$  and  $ODF_{max}$  values indicate that this material is less textured, compared to other investigated samples. By way of contrast, material C reveals a strongly developed Cube texture component with the intensity of 13.94 m.r.d and scattered traces of RD and ND rotated counterparts, while the intensity of other components is negligibly low. Material D is composed of a mixture of Cube and  $\beta$ -fibre orientations of comparable intensities. The investigated non-conventional texture of moderate intensity (material A), weakly textured (material B), Cube dominating (material C), and the mixture of the Cube and  $\beta$ -fibre cover a wide spectrum of hot band textures, which might emerge by altering the TMP parameters during hot rolling.

### 3.2. Cold Rolling Texture

A comparison of Figures 2 and 3 clearly demonstrates that the pre-rolling textures experience severe reorientation. As Figure 3 shows, the evolution of crystallographic texture during 86% thickness reduction imposed by cold rolling occurs mainly along the  $\alpha$ ,  $\beta$  and  $\eta$  fibres. Although all samples were subjected to the same straining degree, both qualitative and quantitative diversities were observed in the textures of investigated materials (see Figures 3 and 4). It is important to underline that the texture of material A became symmetric due to symmetry imposed by conventional/symmetric cold rolling. The unequal distribution of orientations along the  $\alpha$ ,  $\beta$ , and  $\eta$  fibres (Figure 4a–c) is attributed to differences in the hot band textures.

Analyzing the evolution of texture intensities  $f(g)$  along the  $\alpha$ -fibre, one can notice that in all cases the maxima are observed around the Brass orientation (this component also belongs to the  $\beta$ -fibre), while the intensity of Goss component hardly changed. The major qualitative difference between the texture evolutionary patterns in materials A–C and D is related to the presence of  $\{011\}\langle 100\rangle$  in samples A–C, which was not present in the deformed sample D. Apart from this, very weak peaks can be noticed in the vicinity of P-orientation, which can be attributed to the presence of large ( $d \geq 1 \mu\text{m}$ ) non-deformable constituent particles. Results of finite element simulations [7,20] clearly indicate that the deformation flow in the vicinity of the hard inclusions strongly deviates from the particle-free domains and lead to the evolution of orientation spectrum, which is not typical for the plane strain compression (dominant strain mode in rolling).

In materials A–C, which revealed negligibly low (or zero) orientation intensity along the  $\beta$ -fibre in the hot band, the rolling caused a quite homogeneous distribution of components along this fibre. Similar texture distribution was observed in 5xxx Al alloy with almost random pre-rolling texture [7]. The unequal intensity distribution along the  $\beta$ -fibre in material D ( $8 < f(g) < 23.2$ ) is inherited from the HB, which already contained the mentioned deformation texture orientations. After rolling, the intensities of all components in sample D tended to enhance, and the maximum was observed in the vicinity of  $\{314\}\langle 596\rangle$ . The reference orientations of the  $\beta$ -fibre shown in Figure 4b can be computed by the help of expression presented in Figure 1, according to which the position of each individual component of the skeleton line connecting the  $\{112\}\langle 111\rangle$  and  $\{011\}\langle 211\rangle$  in Euler space is a function of a single miller index  $h$  [8]. The intensities of components along the rolling texture fibre in sample D first tend to intensify with an increase of  $h$  from 1 to 3, i.e., while moving from the  $\{112\}\langle 111\rangle$  towards  $\{314\}\langle 596\rangle$ , whereas the  $f(g)$  value follows downward trend by approaching Brass orientation  $\{011\}\langle 112\rangle$  when  $3 < h < \infty$ .

Figures 3 and 4 demonstrate that even a high straining level such as 86% thickness reduction was not capable of ensuring complete reorientation of  $\{001\}\langle 100\rangle$  towards the rolling fibre texture in materials C and D. This is due to the fact that Cube orientation reveals high stability while subjected to plane strain compression. Analysis of  $\eta$ -fibre

(Figure 4c) suggests that materials with initially strong Cube component (C and D) are prone to produce RD rotated Cube orientations such as  $\{014\}\langle 100\rangle$  and  $\{013\}\langle 100\rangle$ .

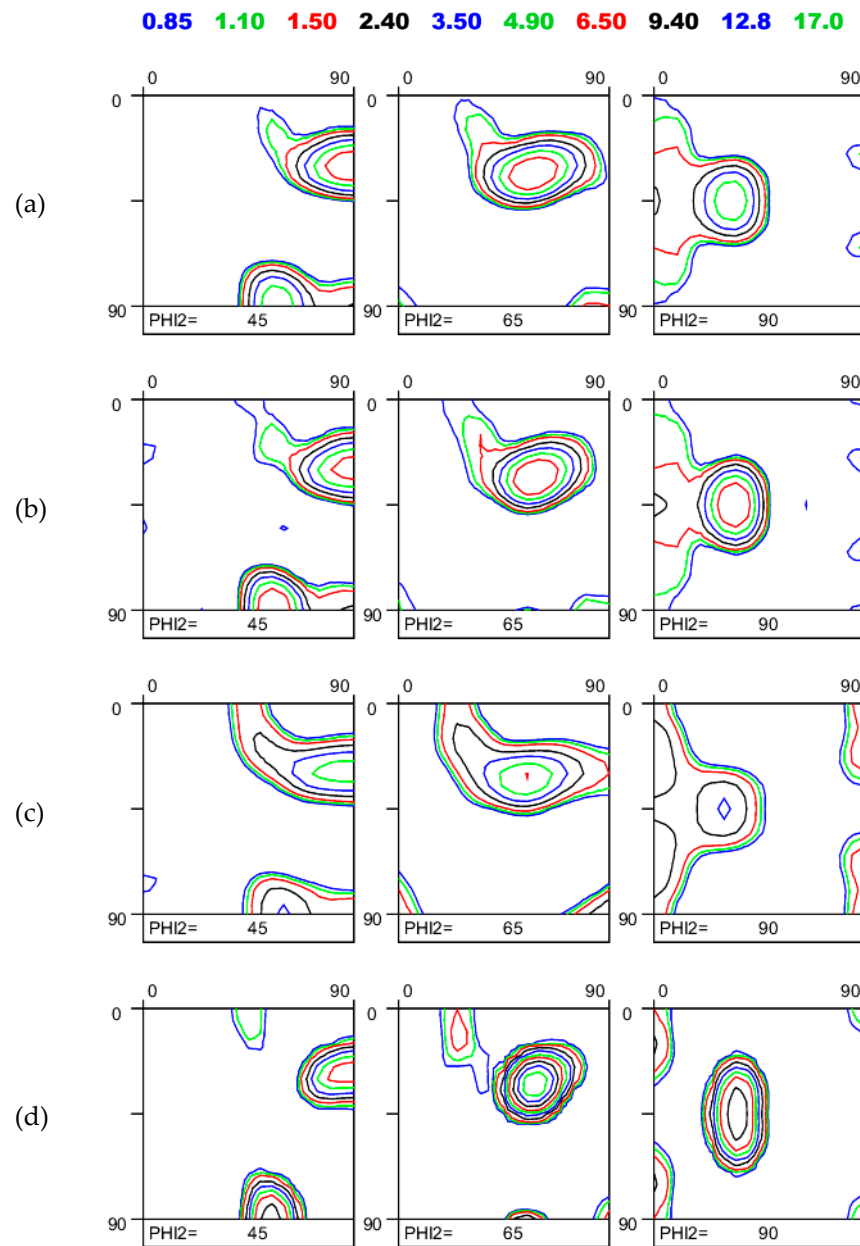


**Figure 3.** Deformation textures after 86% thickness reduction: (a) material A,  $ODF_{max} = 9.03$ ,  $TI = 4.02$ ; (b) material B,  $ODF_{max} = 9.81$ ,  $TI = 4.29$ ; (c) material C,  $ODF_{max} = 6.77$ ,  $TI = 2.88$ ; (d) material D,  $ODF_{max} = 23.16$ ,  $TI = 9.29$ .

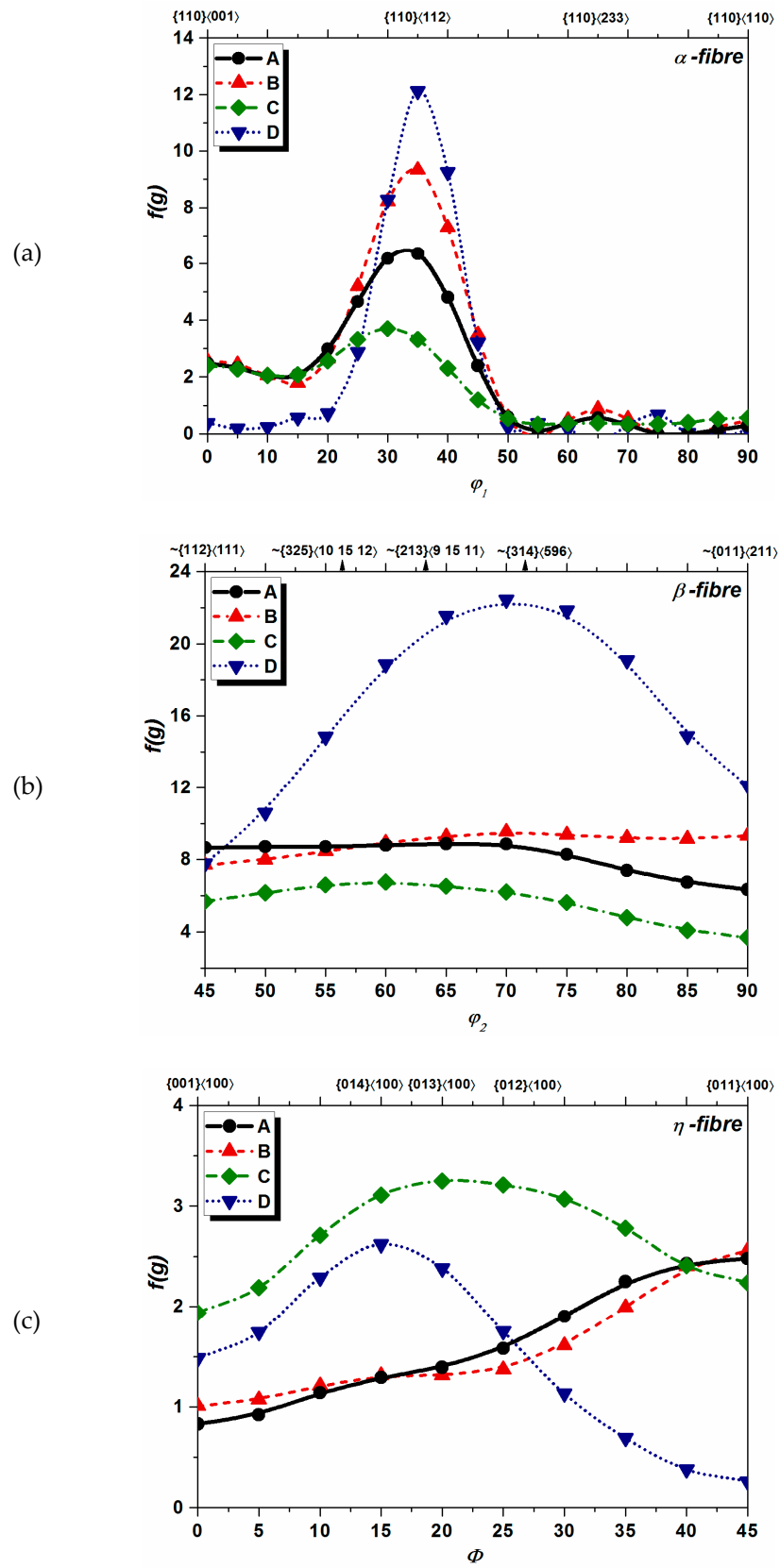
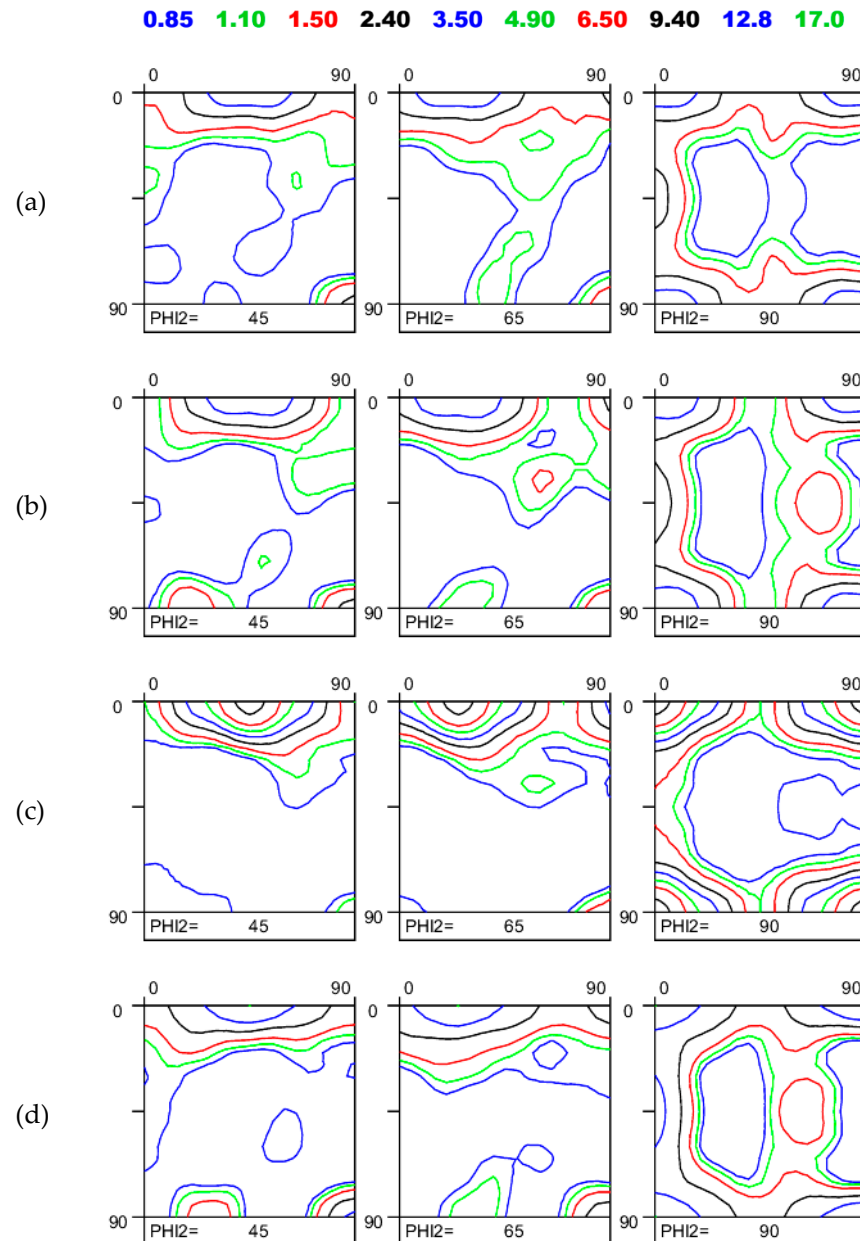


Figure 4. Distribution of orientations along the main texture fibres after 86% thickness reduction: (a)  $\alpha$ -fibre  $\{011\}/\text{ND}$ ; (b)  $\beta$ -fibre; (c)  $\eta$ -fibre  $\{001\}/\text{RD}$ .

### 3.3. Recrystallization Texture

Analysis of ODFs presented in Figures 4 and 5 reveals that the deformation textures experienced severe transformation during recrystallization. As can be seen in Figure 5 both qualitative and quantitative differences are observed in the evolved RX textures of samples A–D since the variety of rolling textures has affected the crystallographic aspect of microstructure development during recrystallization annealing conducted at 550 °C.



**Figure 5.** Recrystallization textures after annealing at 550 °C: (a) material A,  $ODF_{max} = 4.23$ ,  $TI = 1.26$ ; (b) material B,  $ODF_{max} = 4.39$ ,  $TI = 1.36$ ; (c) material C,  $ODF_{max} = 11.03$ ,  $TI = 2.12$ ; (d) material D,  $ODF_{max} = 4.92$ ,  $TI = 1.46$ .

The orientation spectrum in the heat-treated materials A–D is mainly distributed along the  $\alpha$ ,  $\theta$ , and  $\eta$  fibres while other components of lower intensity, such as Q and  $\gamma$ -fibre orientations, are also present in the recrystallized matrix (see Figure 5a–d).

The  $\theta$ -fibre is dominated by the  $\{001\}\langle 100 \rangle$  orientation, whereas the intensity of ND rotated Cube orientations gradually declines while moving towards the 45° rotated

counterpart (H-component). The same evolutionary pattern is observed along the  $\eta$ -fibre where the Cube intensity decreases with the degree of rotation around RD.

Figure 6 presents orientation distribution along the  $\alpha$ ,  $\theta$ , and  $\eta$  fibres. As can be seen in Figure 6a, two peaks appeared in the close vicinity of P and Goss orientation in all investigated materials, while the intensity of other components is relatively weak. Compared to rolled state (Figure 4a), it can be noticed that the intensity of Brass orientation has drastically dropped (vanished) in the RX materials. This is true for all deformation texture components and this drastic qualitative texture change is explained by the mechanism of low stored energy nucleation [7,14,21] when the nuclei of low stored energy (Cube, Goss, P, etc. [7]) consume the domains of high dislocation density.

Detailed examination of Figures 3, 4, 5 and 6 leads to the following conclusive remarks: (i) the deformation texture components of moderate intensities, quite homogeneously distributed along the  $\beta$ -fibre, mixed with the weak RD rotated Cube orientations (Figures 3a,b and 4) induced the evolution of relatively consistent  $\theta$ -fibre, P and Goss texture in materials A and B, while in both cases the intensity of  $\{001\}\langle 100\rangle$  was slightly prevailing over the other  $\theta$ -fibre counterparts; (ii) the Cube- $\beta$ -fibre type of rolling texture (Figures 3c and 4) tended to transform to the Cube dominating RX texture, scattered along the  $\theta$ -fibre (Figures 5c and 6), whereas both the Goss and P orientations revealed low intensities; (iii) in case of strongly developed  $\beta$ -fibre with traces of weak Cube orientation (Figures 3d and 4), the resulting annealing texture was composed of both moderately developed  $\{001\}\langle 100\rangle$  and Goss components, as well as weakly evolved P and E orientations (Figures 5d and 6).

The link between the HB and RX textures is less obvious, however, analysis of ODFs presented in Figures 2c,d and 5c,d suggests that both high and moderate intensities of Cube component in the HB induce similar fraction of this orientation in the recrystallized matrix. This “genetic” link can be explained by experimental observations and numerical approaches [14,21]. Results of experimental evidence [4] claim that the Cube bands are located in-between the rolling texture components and serve to produce a strong Cube texture on annealing. When the HB texture is of low or moderate intensity, the corresponding RX texture is of equivalent intensity, due to the lack of preferable nucleation sites which can ensure the predominance of particular orientations.

Apart from the  $\{001\}\langle 100\rangle$  texture, which usually appears in metals with FCC crystal structure, weak E component, P, Goss, Q ( $\{013\}\langle 231\rangle$ ) and ND rotated Cube orientations tended to evolve in the recrystallized materials A–D (Figure 5a–d). The evolution of these texture components is governed by various annealing phenomena, which take place at microstructural heterogeneities induced by the strain mode heterogeneities in the vicinity of non-deformable particles [2,7,22–24] or in the shear-bands [25]. It should be mentioned that the local events, such as nucleation within the shear bands or particle stimulated nucleation [1,2,7,22–24], which occurs in the particle affected deformation zone, have a great impact on both qualitative and quantitative characteristics of texture evolved during final annealing. These two mechanisms are responsible for the evolution of Goss, E, P, Q, and rotated Cube texture orientations [1,2,7,20,22–26].

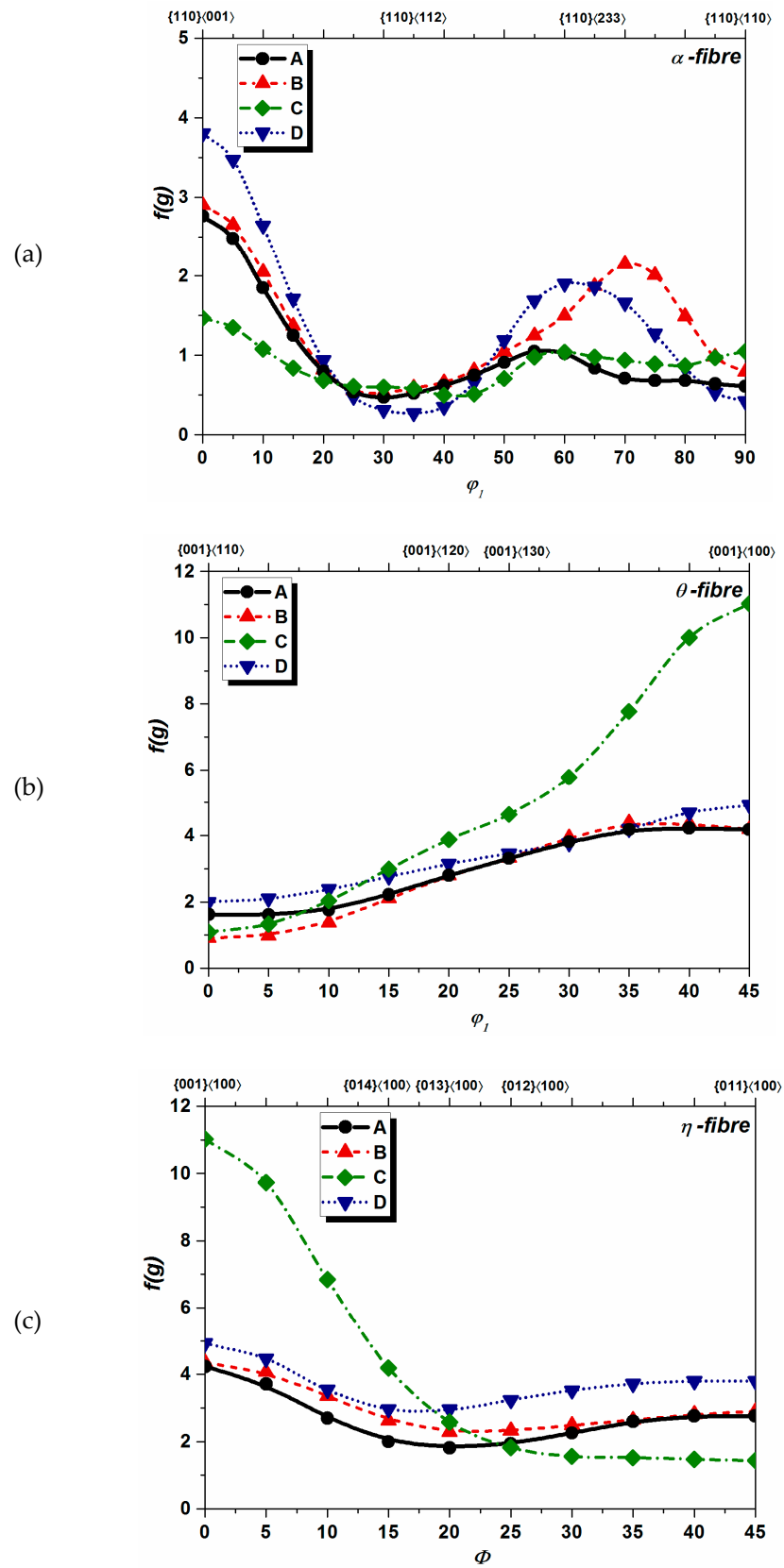


Figure 6. Distribution of orientations along the main texture fibres after annealing at 550 °C: (a)  $\alpha$ -fibre  $\{011\}\langle 110 \rangle$ //ND; (b)  $\theta$ -fibre  $\{001\}\langle 110 \rangle$ //ND; (c)  $\eta$ -fibre  $\{001\}\langle 100 \rangle$ //RD.

The evolution of particular components in the recrystallized matrix can be explained by combining basic principles of continuum mechanics on the grain level and the mobility of grain boundaries. Crystal plasticity simulations [27,28] and modeling approaches developed for RX texture simulation [7,14,21] suggest that the {001}<100> texture is relatively stable during cold rolling and when the material is exposed to annealing this orientation nucleates and grows fast due to low stored energy and high mobility of <111>40° oriented boundaries [21]. In plane strain compression, both Cube and Goss reveal the lowest value of accumulated strain [2,21], and hence, the nucleation occurs via the low stored energy nucleation mechanism [1]. By considering the dominant strain modes that characterize the local displacement fields (mixture of shear, compression, and tension [7,20,21]) within the particle deformation zone and the calculated power dissipation maps [21] for the given deformation modes, it becomes obvious that the Goss, P, and  $\gamma$ -fibre orientations also belong to a low stored energy domain of Euler space. In addition, these components likewise reveal <111>40° orientation relationship with the deformed matrix [14,21]. When it comes to shear bands, the results of crystal plasticity calculations [25] show that the localized shear strain tended to produce P and Q orientations in the deformed grains, and therefore, both texture components can appear in recrystallized materials during the subsequent heat treatment process.

### 3.4. Normal and Planar anisotropy

Numerous studies claim [1,12–16,19] that the crystallographic characteristics of microstructure evolved in a polycrystalline aggregate during TMP induce the anisotropy of mechanical properties such as yield stress, ductility, or Lankford value, and hence, texture control during the entire processing is an important technological challenge. The anisotropy of mechanical properties along the [111], [110] and [100] directions are well documented for single crystals of cubic crystal structure [1] and this phenomenon is explained by the mechanism of deformation. The crystallographic orientation of a single crystal tends to change during the straining depending on the direction of the applied load, whereas the crystal reorientation is conditioned by the neighbors in the polycrystalline matrix. As a consequence of the applied strain mode and activated slip system, even an assembly of randomly oriented crystals will acquire crystallographically preferred texture components, and thus reveal diverse values of mechanical properties in different directions. In view of anisotropic behavior, it is of particular relevance to avoid local thinning of sheets subjected to an arbitrary forming process. The width to thickness reduction ratios (Lankford values), measured in various directions ( $x_i$ ) with respect to RD appear to show evidence of whether a given sheet has a suitable deep drawing quality or not [1,2]. In the most general case, the normal ( $\bar{r}$ ) anisotropy is calculated by the following expression:

$$\bar{r} = \frac{1}{x_n - x_0} \int_{x_0}^{x_n} r(x) dx \approx \frac{1}{2n} (r(x_0) + 2r(x_1) + 2r(x_2) + \dots + r(x_n)) \quad (1)$$

In industrial practice, the  $r$ -values are generally measured at  $x_i = 0^\circ, 45^\circ,$  and  $90^\circ$  with respect to RD, and thus the above equation gains the following form:

$$\bar{r} = \frac{r(0^\circ) + 2r(45^\circ) + r(90^\circ)}{4} \quad (2)$$

The planar anisotropy ( $\Delta r$  value) is conventionally computed by the following expression:

$$\Delta r = \frac{r(0^\circ) - 2r(45^\circ) + r(90^\circ)}{2} \quad (3)$$

Since the  $r$ ,  $\bar{r}$ , and  $\Delta r$  values are not normalized ( $0 \leq r(x_n) \leq \infty$ ,  $0 \leq \bar{r} \leq \infty$  and  $-\infty \leq \Delta r \leq \infty$ ), the comparison of two materials becomes complicated and thus employing

the normalized quantity such as  $q$ -value ( $0 \leq q(x_n) \leq \infty$ ) is more justified. The correlation between the  $r$  and  $q$  values is expressed by Equation (4):

$$q(x_n) = \frac{r(x_n)}{1 + r(x_n)} \quad (4)$$

To assess the in-plane anisotropy, a simple quantity of  $\Delta q$  is introduced [12] as the difference between the maximum ( $q_{max}$ ) and minimum ( $q_{min}$ ) values:

$$\Delta q = q_{max} - q_{min} \quad (5)$$

As an alternative to tensile test measurements, the Lankford profiles can be computed by employing crystal plasticity models, which enable to assess the anisotropy of plastic strain ratio in the recrystallized materials. As shown in various literature sources [2,14–16], the Alamel as well as other Taylor-type homogenization approaches can accurately predict the plastic yielding profiles for materials with distinct textures. Increasing the value of normal anisotropy gives rise to improved plastic behavior of materials in the cup drawing process, which is characterized by the limiting drawing ratio (*LDR*) [29]:

$$LDR = \sqrt{\exp[(2f \exp(-n))\sqrt{(1 + \bar{r})/2}] + \exp[2n\sqrt{(1 + \bar{r})/2}] - 1} \quad (6)$$

where  $f$  is the factor of drawing efficiency ( $f = 0.9$  provides a good correlation between the computed and experimental *LDR* counterparts [29]) and  $n$  is a strain hardening exponent ( $n = 0.26$  in the current case).

The investigated RX textures (see Figure 5) reveal significant varieties that lead to diverse Lankford profiles (see Figure 7). Table 1 presents quantitative indicators of plastic strain ratio, calculated by means of the Alamel model [18,19]. It is obvious that material A appears to reveal the most appropriate deep-drawing characteristics among the investigated samples (see the *LDR* values in Table 1). Comparing the plastic anisotropy qualities by employing conventional  $\bar{r}$  and  $\Delta r$  values might be somewhat misleading since the difference between the  $\Delta r$ -values of materials A and B is quite large ( $\Delta r(A) = 0.09$  and  $\Delta r(B) = 0.17$ ), whereas this difference is not significant while comparing the corresponding  $\Delta q$ -values ( $\Delta q(A) = 0.05$  and  $\Delta q(B) = 0.07$ ). Analysis of Lankford profiles computed for samples A and B (Figure 7) indicates that the  $\Delta q$ -value tends to provide a more reasonable quantity, as compared to  $\Delta r$ . The effect of HB texture on plastic anisotropy can be assessed by examining the  $r$ -curves presented in Figure 7 since both cold rolling and subsequent annealing were performed with identical technological parameters. Inasmuch as the textures of HBs A and B (Figure 2a,b) are weaker in terms of texture intensity, the corresponding Lankford profiles (Figure 7) revealed less anisotropy (see Table 1) compared to samples C and D. It is also apparent from Figure 7 that the large volume fraction of  $\{001\}\langle 100 \rangle$  component in the hot band (Figure 2c,d) accounted for quite pronounced in-plane anisotropy.

**Table 1.** Quantitative characteristics of plastic yielding in the investigated materials A–D.

Material	$\bar{r}$	$\Delta r$	$\bar{q}$	$\Delta q$	<i>LDR</i>
A	0.72	0.09	0.42	0.05	2.06
B	0.67	0.17	0.40	0.07	2.04
C	0.50	0.43	0.33	0.19	1.97
D	0.63	0.20	0.39	0.11	2.02

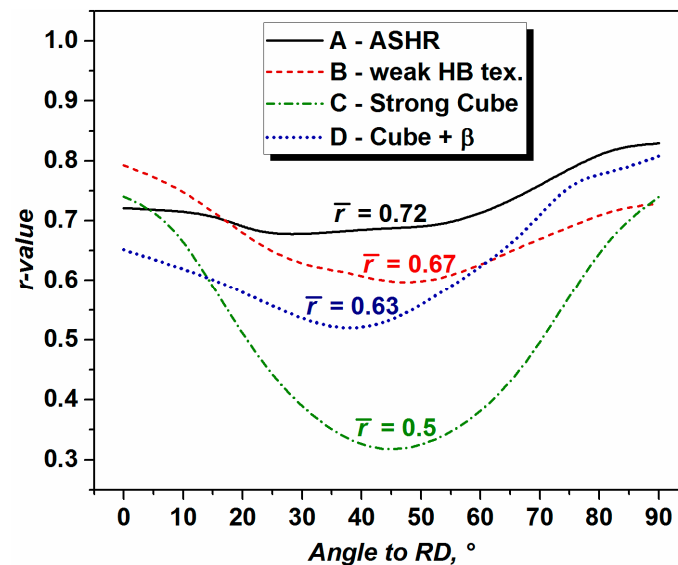


**Figure 7.** Calculated Lankford profiles for investigated materials A–D based on recrystallization textures presented in Figure 5. The legend briefly summarizes the HB textures (ASHR stands for the asymmetrically hot rolled sample with a non-symmetric texture).

In order to clarify the effect of texture components on the planar anisotropy, three qualitatively distinct (characteristic) texture types (Figure 8) were generated and their Lankford profiles were calculated by the Alamel model (Figure 9). The Cube texture of Figure 8a accounted for a symmetric V-shaped profile with a local minimum at 45° with respect to RD. This explains the emerged  $r$ -profile in the investigated material C (Figure 7) with a strongly developed Cube component in the RX matrix. The mixture of Cube and Goss (Figure 8b) did not significantly improve the average value of plastic strain ratio, while the degree of in-plane anisotropy has amplified. It is obvious from Figures 8 and 9 that the presence of Goss orientation in the RX matrix rises the  $r(90^\circ)$  value. Randomizing the texture of Figure 8b by adding the P, Q, and weak E components enhanced the average  $r$ -value, whereas the degree of planar anisotropy improved, compared to the Cube or Cube and Goss dominating ODFs.

Analysis of quantitative indicators of plastic strain ratio presented in Table 2 as well as examination of Lankford curves shown in Figure 9 suggest that recrystallized sheets with the Cube or Cube–Goss type dominating textures are prone to thinning at angles ranging from 30° to 60° to RD. Both Figure 9 and Table 2 lead one to the conclusion that the goal of increasing the  $\bar{r}$  to 1 or even higher with negligible in-plane anisotropy is very challenging, since the set of conventional texture components appearing after final annealing ensures quite strong  $r$ -profiles. Although the  $\bar{r}$  (or  $\bar{q}$ ) and  $\Delta r$  (or  $\Delta q$ ) values are far from ideal in the investigated samples A–D, the current study clearly showed that the behavior of a material during deep drawing can be improved by optimizing the texture evolution in hot rolling. The proper control of other TMP parameters can further enhance the plastic anisotropy indicators in Al alloys.

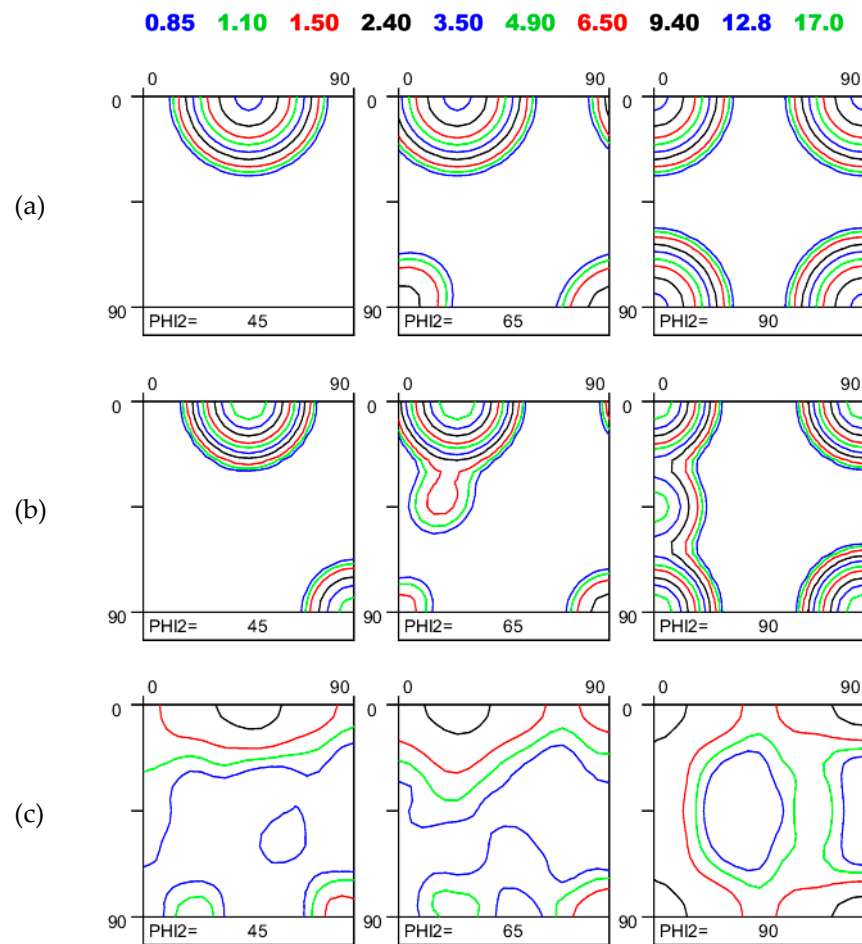


**Figure 8.** Three texture types used for *r*-value calculations, presented in Figure 9: (a) Cube dominated texture; (b) Cube and Goss-type ODF; (c) Cube and Goss mixed with the P, Q and weakly developed E orientation.

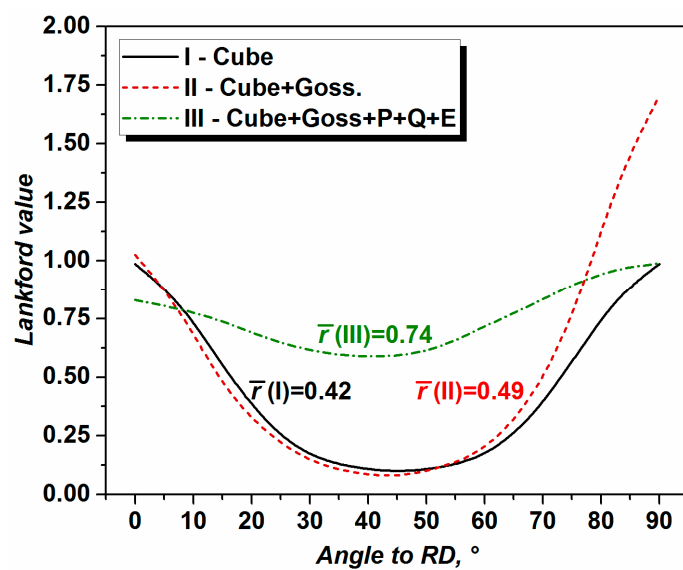


**Figure 9.** Lankford value profiles calculated for three texture types of Figure 8.

**Table 2.** Quantitative indicators of plastic yielding in various texture types shown in Figure 8.

Texture Type	$\bar{r}$	$\Delta r$	$\bar{q}$	$\Delta q$
I. Cube	0.42	0.89	0.28	0.41
II. Cube + Goss	0.49	1.29	0.30	0.56
III. Cube, Goss, P, Q, E	0.74	0.32	0.43	0.13

#### 4. Conclusions

Cold rolling induced a relatively homogeneous distribution of texture components along  $\beta$ -fibre in the weakly textured hot band strips, which primarily revealed negligibly low (or zero) orientation intensity along the given fibre. This type of deformation texture triggered recrystallization texture of moderate intensity. The recrystallization textures of low or moderate intensities tended to ensure relatively flat Lankford profiles with average  $r$ -values ranging between 0.67 and 0.72.

A relatively large fraction of  $\{001\}\langle 100 \rangle$  orientation in the hot bands accounted for the presence of this component in the deformation matrix and finally tended to induce the evolution of Cube dominating recrystallization texture. Crystal plasticity calculations indicate that the strongly developed Cube-type annealing textures served to produce strong V-shaped  $r$ -profiles, which are detrimental for deep drawing.

The asymmetrically hot rolled Al strip, characterized by the non-conventional texture components, and the symmetrically hot rolled counterpart with weakly developed textures are of particular interest since both can give rise to weak recrystallization textures in the cold rolled and subsequently annealed sheets, and thus provide enhanced formability characteristics.

**Author Contributions:** Conceptualization, J.J.S.; methodology, J.J.S.; investigation, J.J.S.; resources, J.J.S.; writing—review and editing, J.J.S.; funding acquisition, J.J.S. The author has read and agreed to the published version of the manuscript.

**Funding:** This research was funded by the EFOP-3.6.1-16-2016-00018 project: “improving the role of research + development + innovation in higher education through institutional developments assisting intelligent specialization in Sopron and Szombathely”. The work was performed in the frame of the Széchenyi 2020 program: “innovative processing technologies, applications of energy engineering, and implementation of wide-ranging techniques for microstructure investigation”.

**Informed Consent Statement:** Not applicable.

**Conflicts of Interest:** The author declares no conflict of interest.

#### References

- Humphreys, J.; Rohrer, G.S.; Rollett, A. *Recrystallization and Related Annealing Phenomena*, 3rd ed.; Elsevier: Amsterdam, The Netherlands, 2017; p. 704.
- Sidor, J.J.; Petrov, R.H.; Kestens, L.A.I. Texture Control in Aluminum Sheets by Conventional and Asymmetric Rolling. In *Comprehensive Materials Processing*; Button, S.T., Ed.; Elsevier: Amsterdam, The Netherlands, 2014; Volume 3, pp. 447–498.
- Engler, O.; Hirsch, J. Texture Control by Thermomechanical Processing of AA6xxx Al–Mg–Si Sheet Alloys for Automotive Applications—A Review. *Mater. Sci. Eng. A* **2002**, *336*, 249–262. [[CrossRef](#)]
- Daaland, O.; Nes, E. Recrystallization Texture Development in Commercial Al–Mn–Mg Alloys. *Acta Mater.* **1996**, *44*, 1413–1435. [[CrossRef](#)]
- Hirsch, J.; Al-Samman, T. Superior light metals by texture engineering: Optimized aluminum and magnesium alloys for automotive applications. *Acta Mater.* **2013**, *61*, 818–843. [[CrossRef](#)]
- Engler, O.; Löchte, L.; Hirsch, J. Through-process simulation of texture and properties during the thermomechanical processing of aluminium sheets. *Acta Mater.* **2007**, *55*, 5449–5463. [[CrossRef](#)]
- Sidor, J.J.; Decroos, K.; Petrov, R.H.; Kestens, L.A.I. Evolution of recrystallization textures in particle containing Al alloys after various rolling reductions: Experimental study and modeling. *Int. J. Plast.* **2015**, *66*, 119–137. [[CrossRef](#)]
- Sidor, J.J.; Kestens, L.A.I. Analytical description of rolling textures in face-centred-cubic metals. *Scripta Mater.* **2013**, *68*, 273–276. [[CrossRef](#)]
- Engler, O. Modelling of Microstructure and Texture and the Resulting Properties during the Thermo-Mechanical Processing of Aluminium Sheets. *Mater. Sc. Forum* **2006**, *519–521*, 1563–1568. [[CrossRef](#)]

10. Hirsch, J. Texture Evolution and Earing in Aluminium Can Sheet. *Mater. Sci. Forum* **2005**, *495–497*, 1565–1572. [[CrossRef](#)]
11. Daaland, O.; Nes, E. Origin of cube texture during hot rolling of commercial Al-Mn-Mg alloys. *Acta Mater.* **1996**, *44*, 1389–1411. [[CrossRef](#)]
12. Kocks, U.F.; Tomé, C.N.; Wenk, H.-R. *Texture and Anisotropy. Preferred Orientations in Polycrystals and Their Effect on Materials Properties*; Cambridge University press: Cambridge, UK, 1998; p. 676.
13. Hutchinson, B. Critical assessment 16: Anisotropy in metals. *Mater. Sci. Technol.* **2015**, *31*, 1393–1401. [[CrossRef](#)]
14. Sidor, J.J.; Petrov, R.H.; Xie, Q.; Van Houtte, P.; Kestens, L.A.I. Evaluation of crystallographic changes and plastic strain ratio in Al alloys. *Mater. Sci. Technol.* **2017**, *33*, 667–677. [[CrossRef](#)]
15. Delannay, L.; Melchior, M.A.; Signorelli, J.W.; Remacle, J.-F.; Kuwabara, T. Influence of grain shape on the planar anisotropy of rolled steel sheets—evaluation of three models. *Comput. Mater. Sci.* **2009**, *45*, 739–743. [[CrossRef](#)]
16. Xie, Q.; Eyckens, P.; Vegter, H.; Moerman, J.; Van Bael, A.; Van Houtte, P. Polycrystal plasticity models based on crystallographic and morphologic texture: Evaluation of predictions of plastic anisotropy and deformation texture. *Mater. Sci. Eng. A* **2013**, *581*, 66–72. [[CrossRef](#)]
17. Yang, X.; Huang, W.; Zhu, X.; Guob, F.; Hu, L.; Zhang, R. The effects of precipitates on microstructure and  $\beta$ -fiber texture in an Al-Cu-Li alloy during hot rolling. *Mater. Charact.* **2020**, *162*, 110186. [[CrossRef](#)]
18. Van Houtte, P.; Li, S.; Seefeldt, M.; Delannay, L. Deformation Texture Prediction: From the Taylor Model to the Advanced Lamel Model. *Int. J. Plast.* **2005**, *21*, 589–624. [[CrossRef](#)]
19. Van Houtte, P.; Kanjarla, A.K.; Van Bael, A.; Seefeldt, M.; Delannay, L. Multiscale Modelling of the Plastic Anisotropy and Deformation Texture of Polycrystalline Materials. *Eur. J. Mech. Solids* **2006**, *25*, 634–648. [[CrossRef](#)]
20. Schafer, C.; Song, J.; Gottstein, G. Modeling of Texture Evolution in the Deformation Zone of Second-Phase Particles. *Acta Mater.* **2009**, *57*, 1026–1034. [[CrossRef](#)]
21. Sidor, J.J.; Petrov, R.H.; Kestens, L.A.I. Modeling the Crystallographic Changes in Aluminum Alloys during Recrystallization. *Acta Mater.* **2011**, *59*, 5735–5748. [[CrossRef](#)]
22. Huang, K.; Li, Y.J.; Marthinsen, K. Factors affecting the strength of P{011}<566> texture after annealing of a cold-rolled Al-Mn-Fe-Si alloy. *J. Mater. Sci.* **2015**, *50*, 5091–5103. [[CrossRef](#)]
23. Huang, K.; Zhang, K.; Marthinsen, K.; Loge, R.E. Controlling grain structure and texture in Al-Mn from the competition between precipitation and recrystallization. *Acta Mater.* **2017**, *141*, 360–373. [[CrossRef](#)]
24. Huang, K.; Marthinsen, K.; Zhao, Q.; Loge, R.E. The double-edge effect of second-phase particles on the recrystallization behaviour and associated mechanical properties of metallic materials. *Prog. Mater. Sci.* **2018**, *92*, 284–359. [[CrossRef](#)]
25. Lapeire, L.; Sidor, J.; Verleysen, P.; Verbeken, K.; De Graeve, I.; Terry, H.; Kestens, L.A.I. Texture comparison between room temperature rolled and cryogenically rolled pure copper. *Acta Mater.* **2015**, *95*, 224–235. [[CrossRef](#)]
26. Duckham, A.; Engler, O.; Knutsen, R.D. Moderation of the Recrystallization Texture by Nucleation at Copper-Type Shear Bands in Al-1Mg. *Acta Mater.* **2004**, *50*, 2881–2893. [[CrossRef](#)]
27. Sidor, J.; Miroux, A.; Petrov, R.; Kestens, L. Microstructural and Crystallographic Aspects of Conventional and Asymmetric Rolling Processes. *Acta Mater.* **2008**, *56*, 2495–2507. [[CrossRef](#)]
28. Sidor, J.J. Assessment of Flow-Line Model in Rolling Texture Simulations. *Metals* **2019**, *9*, 1098. [[CrossRef](#)]
29. Leu, D.-K. Prediction of the Limiting Drawing Ratio and the Maximum Drawing Load in Cup-Drawing. *Int. J. Mach. Tools Manufact.* **1997**, *37*, 201–213. [[CrossRef](#)]